Failure Risk Assessment of Grid-Connected Inverter With Parametric Uncertainty in LCL Filter

Yongyang Chen, *Student Member, IEEE*, Ariya Sangwongwanich, *Member, IEEE*, Meng Huang, *Member, IEEE*, Shangzhi Pan, *Senior Member, IEEE*, Xiaoming Zha, *Senior Member, IEEE*, and Huai Wang, *Senior Member, IEEE*

***Abstract*—Grid-connected inverter failure may be caused by outliers of a population of units in field operation, due to the *LCL* filter parameter uncertainty. This article proposes a probabilistic framework to analyze the impact of multiple filter parameter variances due to component tolerances, operating points, and aging effects. Both robust stability and filter performance are selected as the risk of failure. The robust stability of the grid-connected inverter is quantified by the structured singular value. The total harmonic distortion of the grid current is estimated to evaluate the filter performance. A case study on a three-phase inverter is performed to verify the proposed method through hardware-in-the-loop simulation and physical prototype testing.**

***Index Terms*—Grid-connected inverter, probabilistic assessment, robust stability.**

I. Introduction

In A large-scale renewable energy power plant, there are hundreds or thousands of grid-connected inverters as the interface between renewable energy and the grid [1]. It is almost impossible to design each inverter according to its grid environment and operating condition. Therefore, these inverters usually have the same initial/standard design. Preset worst-case scenarios may be considered in the initial/standard design, but the margin is still difficult to be found for a multiparameter uncertain system [2], especially when component aging is further considered [3]. Therefore, these inverters may be at risk of failure [4].

The robust stability of a grid-connected inverter has been extensively studied [4], [5], [6], [7], [8], [9], [10], [11]. Due to the existence of the resonance point, inverters with *LCL* filters are less robust to parameter variations [5]. Typical uncertain parameters in these studies include grid impedance [5], [6], filter inductance [7], [8], and filter capacitance [9]. Corresponding active damping methods are proposed to improve the robust stability of grid-connected inverters, such as the capacitor current feed-forward (CCF) method [5], [10] and the grid voltage feed-forward method [11].

However, the above methods are for robust stability improvement and cannot quantify the stability margin of a parameter perturbation system [12]. Attempts based on the state-space model and the impedance analysis is carried out to analyze and evaluate the robust stability of an uncertain system [13], [14], [15]. In [13], participation factor analysis is used to assess the harmonic stability of the inverter. This method is based on the eigenvalue sensitivity, which can compare the influence of different state variables but cannot quantify the stability margin. In [14], a black-box method based on impedance measurements is proposed to evaluate the robust stability of the inverter. Fitting the system model with impedance measurements requires knowledge of the system structure and order. Therefore, an improved white-box impedance model is proposed in [15]. The impedance-based method is data-dependent. But, it is difficult to obtain the long-term impedance database for grid-connected inverters under different conditions.

The above robust stability analysis and assessment methods do not consider the distribution characteristics of uncertain parameters, which may lead to an aggressive or conservative result [16]. Due to component tolerances and grid condition differences, the parametric uncertainties of multiple inverters are often given in a distributed form [17]. The aging of component parameters due to the influence of operating conditions also exhibits distribution characteristics [18]. Thus, probabilistic methods are more suitable for quantifying the failure risk of such systems [16]. The mission profile method is widely used in the reliability assessment of components and inverters [18], [19]. The Monte Carlo method with grid condition variations is also applied to the probabilistic stability assessment of inverters [16], [20]. In [21], the comparative study of the μ-analysis and Monte Carlo methods reveals that the μ-analysis method can avoid the time-consuming iterative calculation. However, the effects of environmental stress on the components are not addressed in [21] and the method is only for robust stability.

This article is devoted to developing a probabilistic assessment framework for the failure risk of three-phase

Manuscript received 4 November 2022; revised 2 March 2023; accepted 22 April 2023. Date of publication 8 May 2023; date of current version 21 June 2023. This work was supported in part by the National Natural Science Foundation of China under Grant 52222707. The work of Yongyang Chen was supported by the China Scholarship Council under the State Scholarship Fund (File No. 202106270079). Recommended for publication by Associate Editor S. A. Khajehoddin. *(Corresponding authors: Ariya Sangwongwanich; Meng Huang.)*

Yongyang Chen, Meng Huang, Shangzhi Pan, and Xiaoming Zha are with the Hubei Key Laboratory of Power Equipment and System Security for Integrated Energy, School of Electrical Engineering and Automation, Wuhan University, Wuhan 430072, China (e-mail: yongyang-chen@whu.edu.cn; meng.huang@whu.edu.cn; shangzhi.pan@whu.edu.cn; xmzha@whu.edu.cn).

Ariya Sangwongwanich and Huai Wang are with the Energy Technology, Aalborg University, 9220 Aalborg, Denmark (e-mail: ars@energy.aau.dk; hwa@et.aau.dk).

Color versions of one or more figures in this article are available at https://doi.org/10.1109/TPEL.2023.3274396.

Digital Object Identifier 10.1109/TPEL.2023.3274396

TABLE I
PROBABILISTIC ASSESSMENT ATTEMPTS FOR INVERTER PERFORMANCE

Assessment	Uncertainty	Method	Failure Criterion
Reliability [18][19]	Component aging	Mission profile	Accumulated damage
Robust stability [16][20]	Operational conditions	Monte Carlo	Eigenvalue or Nyquist
Failure risk (proposed framework)	Tolerance, aging, conditions	Mission profile, μ-analysis and Monte Carlo	SSV and THD

grid-connected inverters. Both robust stability and filter performance are selected as the risk of failure. If the index of stability (SSV) or filter performance (THD) exceeds the criterion, the inverter is deemed to be in failure. The concept of uncertainty quantification (UQ) is proposed to reduce the risk caused by uncertainty [22]. In [17], parametric uncertainty is quantified in the design process of the inverter to reduce its impact on design objectives. In this article, the degree to which parametric uncertainty affects the failure risk are investigated via UQ. The comparison between the proposed framework and the conventional probabilistic assessment attempts is given in Table I. It reveals from Table I that the main differences and contributions of the proposed framework are as follows.

1) The impact of multiple filter parameter variances due to component tolerances, operating points, and aging effects are quantified in the proposed probabilistic framework. The influence of environmental stress on robust stability and filter performance is analyzed based on the mission profile method.
2) In this article, both robust stability and filter performance are selected as the risk of failure. The failure risk of grid-connected inverters is determined by the performance index with the highest risk. Thus, the proposed risk assessment framework can be easily extended to more performance indexes.

In Section II, the sources of parametric uncertainties are investigated, and parametric uncertainties are quantified based on mechanism analyses and data fitting. In Section III, based on the structured singular value analysis, the stable parameter domain of the grid-connected inverter is determined. Combining the stable parameter domain and the uncertain parameter distribution, the instability risk of the inverter is quantified. Then, the total harmonic distortion (THD) of the grid current is estimated to assess the risk of poor filter performance. Finally, the probabilistic assessment framework of the grid-connected inverter's failure risk is proposed. Case studies and experimental verifications are presented in Section IV and Section V, respectively. The summary and conclusion are in Section VI.

II. PARAMETRIC UNCERTAINTY QUANTIFICATION

The block diagram of the grid-connected inverter is shown in Fig. 1, and the nominal parameters are given in Table II. The blue dotted line in Fig.1 indicates the power hardware part, and the rest is the sampling, control, and modulation part. Uncertain parameters and their nominal values are represented by lowercase and uppercase letters, respectively. This article considers uncertain parameters from passive components, including filter inductance l_1, capacitance c_f, and grid inductance l_g.

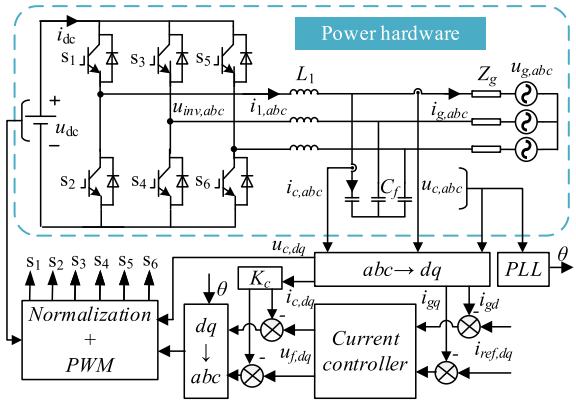

Fig. 1. Block diagram of three-phase *LCL*-filtered grid-connected inverter.

TABLE II
NOMINAL PARAMETERS OF THE INVERTER

System parameters	Symbol	Nominal Value
System capacity	S_{inv}	6600 VA
DC voltage	u_{dc}	800 V
Grid voltage (RMS)	u_g	220 V
Filter inductance	L_1	2.4 mH
Filter capacitance	C_f	10 μF
Sampling frequency	f_s	10 kHz
Grid resistance	R_g	0.1 Ω
Grid inductance	L_g	0.9 mH
Controller coefficients	K_p /K_i	0.4/40

For grid-connected inverters, parameter uncertainties are mainly introduced by parameter tolerance of component manufacturing, parameter deviation of component aging, and uncertainty of operational conditions [3]. In addition, the influence of environmental stress on component parameters is studied in this section. Based on mechanism analyses and measurement data, parametric UQ can be obtained through theorem derivation and data fitting.

A. Tolerance From Production

Components deviate from their nominal parameters due to constraints of the production process. The component tolerance represents the degree to which a component parameter deviates from the nominal parameter. For example, the filter inductor tolerance can be more than 15% [23], and the filter capacitor tolerance is typically in the range of 5% to 10% [24].

The central limit theorem indicates that the uncertainty affected by multiple independent random factors tends to be in a normal distribution [25]. The probability density function (PDF)

TABLE III
FILTER INDUCTOR PARAMETERS

Parameters	Symbol	Value
Initial inductance	L_1	2.352 mH
Magnetic path length	l_e	0.243 m
Number of turns	N	99
Fit formula parameters	a / c	0.01 / 1.819
Fit formula parameter	b	$7.98{\cdot}10^{-7}$

of a normal distribution is known as

$$f(e) = \frac{1}{\sqrt{2\pi(\sigma)^2}} \cdot \exp\left[-\frac{1}{2} \cdot \left(\frac{e-E}{\sigma}\right)^2\right] \tag{1}$$

where the lowercase e is a random variable, the uppercase E is the expectation, and σ is the standard deviation.

The normal distribution in (1) is recorded as $e \sim N(E, \sigma)$.

B. Uncertainty of Operational Conditions

Under normal conditions, the output power of an inverter is between full load and no load. Due to the soft saturation of the magnetic core, the parameter of the filter inductor will be affected by the operating point [26]. Taking the powder core as an example, the soft saturation characteristics of the filter inductance are expressed as follows [27]:

$$\text{initial permeability}(\%) = \frac{1}{a + b(iN/l_e)^c} \tag{2}$$

where i is the current flowing through the filter inductor. a, b, and c are fit formula parameters. N is the number of turns and l_e is the magnetic path length.

For the filter inductor in this article, the corresponding values in (2) are given in Table III [7]. According to (2), if the full load current of the inverter is 20 A, the corresponding permeability will be 88.7%. Combined with the inductor tolerance from production, the perturbation range of the filter inductance is set to $\pm 30\%$. For a typical normal distribution, more than 99% of the parameters are distributed within plus or minus three times the standard deviation of the expected value. Thus, the standard deviation of the filter inductance is set to 10%, that is $l_1 \sim N(L_1, 10\%L_1)$.

Compared with filter inductors, the distribution of grid inductance is more complex. The grid inductance is different for different installation positions and grid conditions. According to the measurements in [20], the grid impedance approximately exhibits a normal distribution in the logarithmic coordinate. Therefore, it can be assumed that $\ln(l_g) \sim N(E_g, \sigma_g)$. The expectation and standard deviation of the logarithmic normal distributed parameter l_g are recorded as $E(l_g)$ and $\sigma(l_g)$ [28]

$$E(l_g) = \exp\left[E_g + \sigma_g^2/2\right] \tag{3}$$

$$\sigma(l_g) = \left[\exp\left(\sigma_g^2\right) - 1\right] \times \exp\left(2E_g + \sigma_g^2\right). \tag{4}$$

The PDF of the lognormal distribution under different parameters is shown in Fig. 2. It can be seen that when the standard deviation is $0.125L_g$, the lognormal distribution is close to the normal distribution. When the standard deviation is higher, the logarithmic normal distribution has more values distributed upwards. This is in line with the weak grid situation.

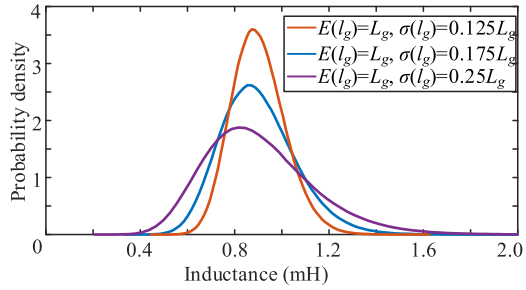

Fig. 2. PDF of the lognormal distribution under different parameters.

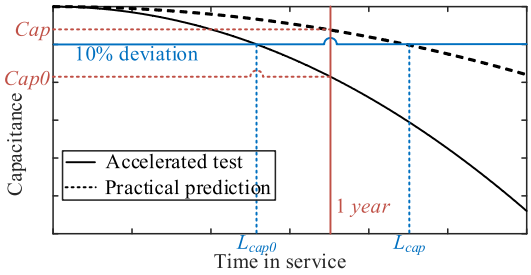

Fig. 3. Schematic diagram of filter capacitance aging prediction from the accelerated test.

C. Deviation With Aging

The metalized film capacitor is often used in *LCL* filters because of its high electric-field stress [29]. The failure mechanism of metalized film capacitors has been extensively studied in related reliability researches [25], [29]. Due to dielectric breakdown, aging of the metalized film capacitor results in capacitance loss [25], as shown in Fig. 3. The failure of film capacitors is mainly affected by the voltage, temperature, and humidity [30]. The influence of these factors on the capacitor's lifetime can be expressed by the Arrhenius–Peck relation [31]

$$L_{\text{Cap}} = L_{\text{Cap0}} \times KL \tag{5}$$

$$KL = \left(\frac{V_{\text{cap}}}{V_{\text{cap0}}}\right)^{-p_1} \times \exp\left[\left(\frac{1}{T_{\text{cap}}} - \frac{1}{T_{\text{cap0}}}\right)\frac{E_a}{K_B}\right] \times \left(\frac{RH}{RH_0}\right)^{-p_2} \tag{6}$$

where L_{cap0} is the lifetime in the accelerated test and L_{cap} is the lifetime prediction for the applied condition. V_{cap}, T_{cap}, and RH are the voltage, temperature, and humidity for the applied condition, respectively. V_{cap0}, T_{cap0}, and RH_0 are the reference conditions in the accelerated test. The meanings and values of the remaining coefficients are given in Table IV [31].

According to the accelerated test data in [30], the capacitance distribution of thin film capacitors during the aging process can be fitted with a Weibull distribution. The PDF of a Weibull

TABLE IV
COEFFICIENTS IN ARRHENIUS–PECK RELATION FOR FILM CAPACITORS

Coefficients	Symbol	Value
Activation energy	E_a	0.6 *eV*
Boltzmann's constant	K_B	$8.62 \cdot 10^{-5}$ *eV/K*
Voltage stress coefficient	$-p_1$	-9
Humidity stress coefficient	$-p_2$	-2.66

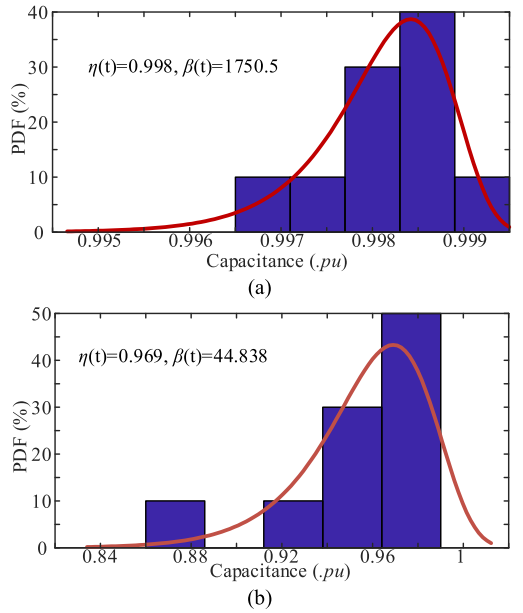

Fig. 4. Weibull fitting from the accelerated test. (a) 210 h. (b) 1449 h.

distribution is known as follows [29]:

$$f_C(c) = \frac{\beta}{\eta} \cdot \left(\frac{c}{\eta}\right)^{\beta-1} \cdot \exp\left[-\left(\frac{c}{\eta}\right)^{\beta}\right] \tag{7}$$

where the lowercase c is the random variable, η is the scale parameter, and β is the shape parameter.

The Weibull fitting of the accelerated test at 85 °C (358.15 Kelvin), 400 V, and 85% relative humidity is shown in Fig. 4 [30]. It can be seen from Fig. 4 that as the test time increases, the capacitance of the film capacitor decreases, and the variance of the capacitance distribution increases. The Weibull distribution in (7) is recorded as $c \sim Wb(\eta, \beta)$. The aging process in the accelerated test can be represented by a Weibull distribution with time-dependent parameters $c_{f0}(t) \sim Wb(\eta_0(t), \beta_0(t))$.

As shown in Fig.3, take the accelerated test as a reference, the lifetime of use conditions can be predicted with (5). The predicted capacitance distribution for use conditions can be expressed as follows, considering the mission profile of the applied condition

$$c_f \sim Wb\left(\eta_0\left(\frac{t}{KL}\right), \beta_0\left(\frac{t}{KL}\right)\right) = Wb(\eta(t), \beta(t)) \tag{8}$$

The predicted distribution of the filter capacitance at 50 °C, 400 V and 35% relative humidity is shown in Fig. 5. Similar to

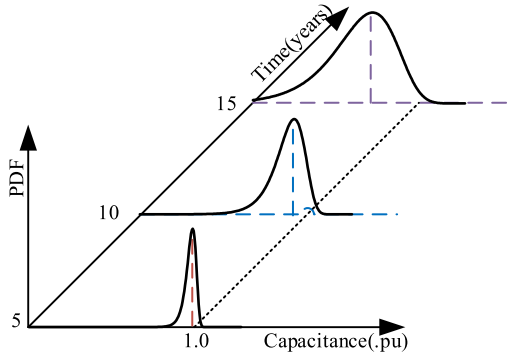

Fig. 5. Parametric UQ of the filter capacitance.

Fig. 4, the filter capacitance gradually decreases and the range of capacitance distribution gradually increases with aging.

For the *LCL* filter, the aging deviation of the filter capacitor is relatively obvious [18]. Thus, this section mainly analyzes the aging process of the filter capacitor. The mission profile in this section is also limited, but the methods and procedures for failure risk assessment remain the same with more complex mission profiles.

III. PROBABILISTIC ASSESSMENT FRAMEWORK

In this article, robust stability and filter performance are selected as the performance indicators of the inverter's failure risk. The structured singular value and THD of grid current are used as the assessment indexes of robust stability and filter performance, respectively. The corresponding assessment framework is proposed as follows.

A. Robust Stability Assessment

The robust stability model of the uncertain system is based on the nominal system model. The closed-loop block diagram of the *LCL*-filtered three-phase inverter in the synchronous frame is shown in Fig. 6 and the blocks of uncertain parameters are marked in blue. To improve the robust stability of the inverter, the active damping strategy with CCF is applied and the CCF coefficient is K_c.

The current control in the synchronous frame adopts a PI regulator. The controller outputs of the d-axis and q-axis are denoted as u_{fd} and u_{fq}, respectively. The controller state variables are defined as x_1, x_2

$$x_1 = u_{fd} - K_{pd} i_{gd}^* \tag{9}$$

$$x_2 = u_{fq} - K_{pq} i_{gq}^* \tag{10}$$

where K_{pd} and K_{pq} are the proportional coefficients of the d-axis regulator and the q-axis regulator, respectively.

The state-space equations of the PI regulators in the synchronous frame are

$$\begin{bmatrix} \dot{x}_1 \\ \dot{x}_2 \end{bmatrix} = \begin{bmatrix} K_{id} & 0 \\ 0 & K_{iq} \end{bmatrix} \begin{bmatrix} i_{gd}^* \\ i_{gq}^* \end{bmatrix} \tag{11}$$

where K_{id} and K_{iq} are the integral coefficients of the d-axis regulator and the q-axis regulator, respectively.

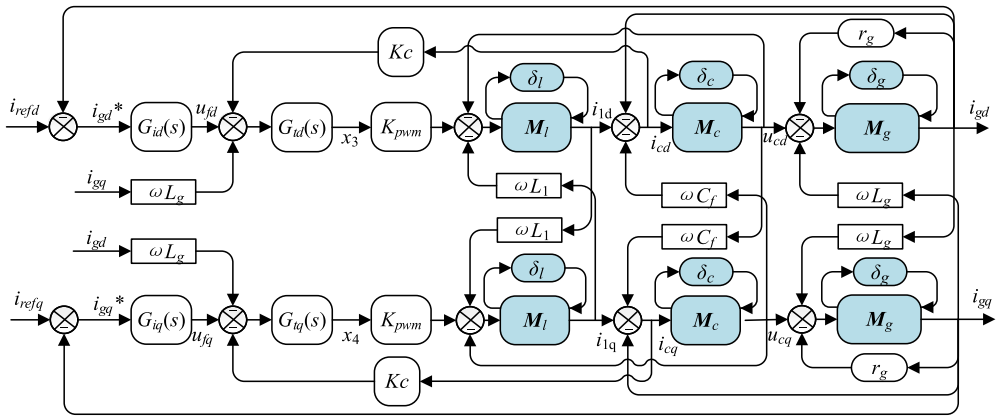

Fig. 6. Closed-loop block diagram of the *LCL*-filtered inverter with multiple uncertain parameters.

The time delay modules of d-axis and q-axis are denoted as $G_{td}(s)$ and $G_{tq}(s)$, respectively. The time delay adopts a one-order Taylor expansion [32]. The outputs of the time delay modules are defined as x_3 and x_4, respectively. In inverters, the time delay mainly comes from the controller and modulation [33]. For ease of expression, the theoretical derivation section of this article combines controller delay and modulation delay. The delay time is defined as T_d. The sampling period is recorded as T_s and the default value of T_d is $1.5T_s$.

In the synchronous frame, the state vector is defined as $\boldsymbol{x} = [i_{1\mathrm{d}}, i_{1\mathrm{q}}, i_{gd}, i_{gq}, u_{cd}, u_{cq}, x_1, x_2, x_3, x_4,]^T$. The output vector is defined as $\boldsymbol{y} = [i_{gd}, i_{gq}]^T$ and the input vector is $\boldsymbol{u} = [u_{gd}, u_{gq}, i_{\mathrm{ref}d}, i_{\mathrm{ref}q}]^T$. Thus, the nominal state-space model of the *LCL*-filtered grid-connected inverter is as follows:

$$\begin{bmatrix} \boldsymbol{y} \\ \dot{\boldsymbol{x}} \end{bmatrix} = \begin{bmatrix} \boldsymbol{O} & \boldsymbol{C} \\ \boldsymbol{B} & \boldsymbol{A} \end{bmatrix} \begin{bmatrix} \boldsymbol{u} \\ \boldsymbol{x} \end{bmatrix} \tag{12}$$

where $\boldsymbol{A}$ is the state matrix, $\boldsymbol{B}$ is the input matrix, and $\boldsymbol{C}$ is the output matrix. Specific matrices can refer to Appendix A. The matrix $\boldsymbol{O}$ has appropriate dimensions and all elements are 0.

Uncertain parameters studied in this article include filter inductance l_1, filter capacitance c_f, and grid inductance l_g. The uncertain parameter model is a product perturbation model. Taking filter inductance l_1 as an example, the product perturbation model of l_1 is

$$l_1 = L_1 \left(1 + P_l \delta_l\right) \tag{13}$$

where L_1 is the nominal value of the filter inductance, and P_l is the maximum parameter perturbation percentage of L_1. The uncertainty δ_l is bounded between -1 to 1 for the normalization of stability criteria.

The perturbation percentages of filter capacitance c_f, and grid inductance l_g, are denoted as P_c, and P_g, respectively. The uncertainties of c_f and l_g are denoted as δ_{c} and δ_g, respectively.

To apply the structured singular value analysis, the uncertainties should be separated from the known part of the system. This separation can be achieved by the linear fractional transformation (LFT) method [34]. The upper LFT forms of $1/l_1$, $1/c_f$, and $1/l_g$ are donated as F_u ($\boldsymbol{M}_l$, δ_l), F_u ($\boldsymbol{M}_c$, δ_{c}), and F_u [$\boldsymbol{M}_g$, δ_{g}], respectively. For the specific calculation of the LFT method and the structure of the coefficient matrices, please refer to [21].

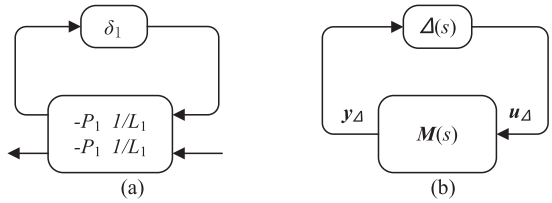

Fig. 7. Uncertain models. (a) Uncertain parameter model. (b) General uncertain system model.

The models of the uncertain parameter and uncertain system are shown in Fig. 7. The uncertainty matrix $\Delta(s)$ is as follows:

$$\Delta\left(s\right) = \mathrm{diag}\left(\delta_1, \delta_1, \delta_g, \delta_g, \delta_c, \delta_c\right). \tag{14}$$

The input vector of the uncertainty matrix $\Delta(s)$ is defined as $\boldsymbol{y}_\Delta$ and the output vector of $\Delta(s)$ is defined as $\boldsymbol{u}_\Delta$. The extended state-space model is expressed as

$$\begin{bmatrix} \boldsymbol{y}_\Delta \\ \dot{\boldsymbol{x}} \end{bmatrix} = \begin{bmatrix} \boldsymbol{D}_{11} & \boldsymbol{C}_1 \\ \boldsymbol{B}_1 & \boldsymbol{A} \end{bmatrix} \begin{bmatrix} \boldsymbol{u}_\Delta \\ \boldsymbol{x} \end{bmatrix} \tag{15}$$

where the state matrix $\boldsymbol{A}$ is the same as that in (12). The remaining matrices can be calculated by the LFT method and specific matrices can refer to Appendix B.

The transfer function matrix $\boldsymbol{M}(s)$ can be derived from the extended state-space model (15)

$$\boldsymbol{M}\left(s\right) = \boldsymbol{C}_1(s\boldsymbol{I} - \boldsymbol{A})^{-1}\boldsymbol{B}_1 + \boldsymbol{D}_{11} \tag{16}$$

where $\boldsymbol{I}$ is an identity matrix.

For the general uncertain system model shown in Fig. 7(b), the structured singular value can be calculated by the MATLAB robust toolbox [35]. The SSV of $\boldsymbol{M}(s)$ in (16) is recorded as $\mu_\Delta(\boldsymbol{M})$ and the maximum SSV is recorded as μ.

For the convenience of expression, the uncertain parameters are recorded as g_1, g_2 and so on. The corresponding nominal parameters of g_i ($i = 1, 2\ldots$) are recorded as G_i and the perturbation range of g_i is recorded as P_i. According to [21],

TABLE V
THD ESTIMATION

Capacitance (μF)	THD Estimation (%)	THD with FFT (%)
12	3.13	2.77
10	3.80	3.61
8	5.07	5.1
6	6.98	10.0

the robust stability domain based on the SSV method is a hypercube in the multidimensional parameter space. The stability margin of the SSV method is $1/\mu$. The upper and lower bound of the hypercube are $G_i\,(1 + P_i\,/\mu)$ and $G_i\,(1\text{-}P_i\,/\mu)$, respectively. The probability that the system is stable is the probability that the uncertain parameters are within the hypercube

$$Q(r) = \prod_{i=1}^{k} Q\left(G_i\left(1 - P_i/\mu\right) \le g_i \le G_i\left(1 + P_i/\mu\right)\right) \quad (17)$$

where $Q(X)$ represents the probability of event X.

B. Filter Performance Assessment

Despite stability, the parameter deviations of the *LCL* filter will also influence filter performance. The failure of filter performance will result in excessive harmonics of grid current. Therefore, the THD of grid current is used as the index to quantify the filter performance. According to [36], the THD of grid-connected current can be estimated as follows:

$$\mathrm{THD} = \frac{1}{24}\frac{v_{\mathrm{dc}}}{f_{sw}L_1L_gC_f}\frac{1}{\left(m_f-6\right)^2\omega_n^2 - \omega_{\mathrm{res}}^2} f\left(m\right) \quad (18)$$

$$f\left(m\right) = \sqrt{\frac{3}{2}m^2 - \frac{3\sqrt{3}}{\pi} + \frac{9}{8}\left(\frac{3}{2} - \frac{9\sqrt{3}}{8\pi}m^4\right)} \quad (19)$$

where m is the modulation ratio. $\omega_n = 2\pi f_n$ is the grid frequency, and f_{sw} is the switching frequency. $m_f = f_{sw}/f_n$. ω_{res} is the resonance frequency for the *LCL* filter.

When the filter capacitance changes (L_g = 0.6 mH, L_1 = 2.4 mH), the THD estimation by (18) and the corresponding FFT analysis of simulation are given in Table V. THD exceeding 5% is used as the criterion for filter performance failure. Since the error around the criterion is small, the accuracy of the filter performance assessment is acceptable.

The filter performance assessment process adopts the Monte Carlo method. First, a large number of parameter groups are generated according to the parameter distribution in Section II. The number of parameter groups is recorded as N_P. Subsequently, the corresponding THD estimation of each parameter group is calculated with (18). Third, the number of parameter groups with a THD less than 5% is obtained by statistics, and the total number of eligible groups is recorded as *Num*. Finally, the risk of THD exceeding 5% can be obtained as follows:

$$F_{\mathrm{THD}} = 1 - \frac{\mathrm{Num}}{N_P}. \quad (20)$$

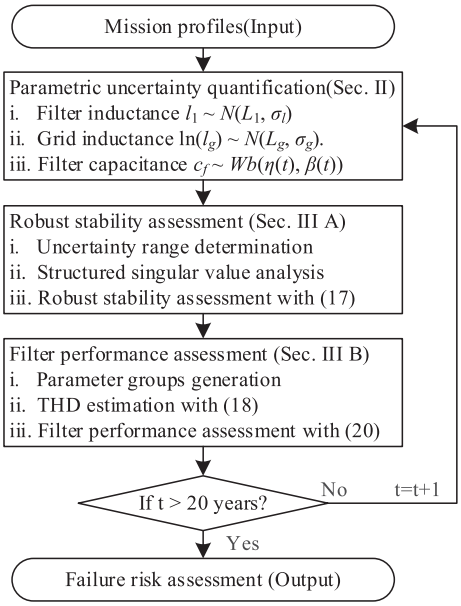

Fig. 8. Failure risk assessment procedure.

C. Failure Risk Assessment Procedure

The failure risk assessment procedure is shown in Fig. 8. The input of the assessment is the component tolerance range and operating condition investigated in Section II. The known component tolerance and operating condition can quantify the parametric uncertainties through mechanism analyses and data fitting. According to Section II, the filter inductance and grid inductance distributions are time-independent, while the filter capacitor distribution is time-dependent. Combined the parametric UQ, the robust stability and filter performance are analyzed, and the corresponding assessment results are obtained. Then, it checks if the life expectancy is reached. If no, the subsequent evaluation is performed; if yes, the assessment result is counted. The final output is the failure risk assessment of the grid-connected inverter within the expected life. The failure risk of grid-connected inverters is determined by the performance index with the highest risk. The proposed assessment framework can be extended to more performance indexes or other filter topologies.

IV. CASE STUDY

This section presents the results of three cases considering different sources of uncertainty. The nominal parameter of the inverter is given in Table II. The corresponding uncertain parameter distributions of these cases are given in Table VI. case 1 considers the uncertainty from component tolerance; case 2 includes the additional effect from component operating conditions, and Case 3 adds the impact of component aging. The mission profile of case 3 is the same with that of Fig. 5.

The maximum SSV and the THD of the grid current are shown in Fig. 9 by taking case 2 as an example. When the parameter increases, the filtering performance improves, and the THD of the grid current decreases. The variation range of each parameter

TABLE VI
UNCERTAIN PARAMETER DISTRIBUTION

	Case 1	Case 2	Case 3
Source of Uncertainty	Tolerance	Tolerance and weak grid	Tolerance, weak grid and aging
Filter ind.	$l_1 \sim N(L_1, 10\%L_1)$	$l_1 \sim N(L_1, 10\%L_1)$	$l_1 \sim N(L_1, 10\%L_1)$
Grid ind.	$l_g \sim N(L_g, 10\%L_g)$	$l_g \sim lnN(L_g, 25\%L_g)$	$l_g \sim lnN(L_g, 25\%L_g)$
Filter cap.	$c_f \sim N(C_f, 3\%C_f)$	$c_f \sim N(C_f, 3\%C_f)$	$c_f \sim Wb(\eta(t), \beta(t))$

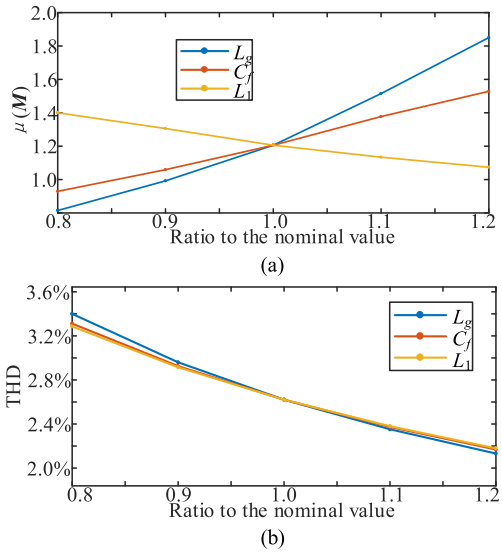

Fig. 9. Analysis results when parameters vary. (a) Structured singular value. (b) Total harmonic distortion.

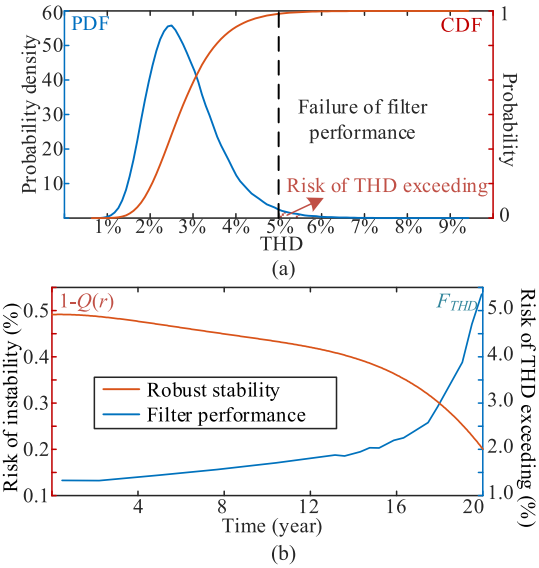

Fig. 10. Assessment results. (a) THD distribution of case 2. (b) Failure risk assessment of case 3.

TABLE VII
FAILURE RISK ASSESSMENT RESULTS

	Case 1	Case 2	Case 3
Structured singular value	0.69	1.21	1.21 to 0.97
Risk of instability (1-$Q(r)$)	<0.01%	0.49%	0.49% to 0.21%
Risk of THD exceeding 5% (F_{THD})	0.07%	1.35%	1.35% to 5.44%

in Fig. 9(b) is limited, so the THD of the grid current does not exceed the criterion for filter performance failure (THD = 5%). The parameter range constrained by the filtering performance can be further obtained by reducing each parameter. For SSV, increasing grid inductance and filter capacitance will increase the maximum SSV, which increases the risk of instability. However, increasing the filter inductance reduces the risk of instability.

The robust stability domain in this article is a cube in the three-dimensional parameter space and the instability risk is the probability that the uncertain parameters are beyond the cube. The risk of THD exceeding can be directly estimated by the Monte Carlo method. For case 2, the THD distribution of the grid current is shown in Fig. 10(a) and the risk of THD exceeding is the integral of the distribution function greater than 5%. Further, the failure risk assessment of case 3 is shown in Fig. 10(b). Due to the influence of the filter capacitor aging, the instability risk will decrease with the running time, while the risk of THD exceeding will increase.

The assessment result of each case is given in Table VII. Compared with case 1, due to the increased distribution range of grid inductance, the instability risk and the THD exceeding risk of case 2 are significantly increased. The uncertain parameter distributions of case 3 at the initial moment are the same as those of case 2. Therefore, the assessment results of case 3 at the initial moment are the same as those of case 2.

The failure risk assessment of case 3 shown in Fig. 10(b) is just for one kind of mission profile. More assessment results under different temperatures and relative humidity levels are shown in Fig. 11. It can be seen from Fig. 11(a) that when the operational temperature is higher, the risk of instability decreases faster. Relative humidity has the same effect on the risk of instability. However, the risk of THD exceeding rises faster at a higher operating temperature or relative humidity. This shows that with the aging of the filter capacitor, the THD of grid current is more likely to exceed the standard.

According to the analysis in Fig. 9, the *LC* filter can be redesigned to limit the risk of THD exceeding within acceptable levels. The redesigned cases with a higher nominal capacitance (12 μF) and a higher filter inductance (3.0 mH) are shown in Fig. 12(a) and (b), respectively. Although increasing the filter capacitor can reduce the risk of THD exceeding, it also increases the risk of instability. Meanwhile, increasing the filter inductance can improve the robust stability and filter performance of the system at the same time. Therefore, increasing the filter inductance is a better choice to reduce the risk of THD exceeding. For nominal value design, because the aging process of the filter capacitor is relatively obvious, it is more appropriate to select the nominal value with a lower sensitivity of filter capacitance.

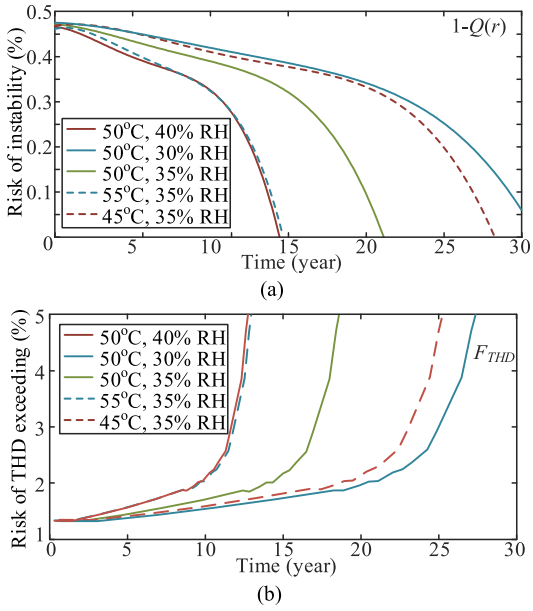

Fig. 11. Assessment results with different temperatures and relative humidity levels. (a) Risk of instability. (b) Risk of THD exceeding.

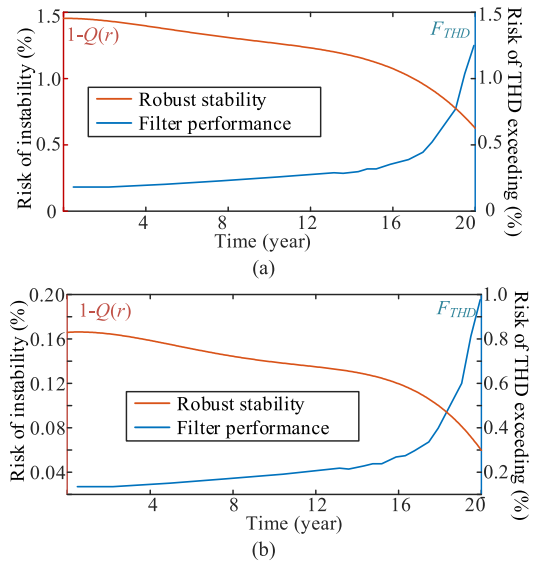

Fig. 12. Failure risk assessment results for redesigned cases. (a) Redesigned case with a higher filter capacitance (12 μF). (b) Redesigned case with a higher filter inductance (3.0 mH).

V. Verifications

The HIL simulation platform with Typhoon 402 and the physical prototype of a three-phase inverter are shown in Fig. 13(a) and (b), respectively. The controller is DSP 28335, and the nominal parameters of HIL simulation are given in Table II. For the HIL simulation, the power hardware in the blue dotted line of Fig. 1 is simulated in Typhoon HIL device, while the rest of the control and modulation parts are realized by the DSP controller board. Such a simulation structure is also called controller hardware-in-the- loop simulation.

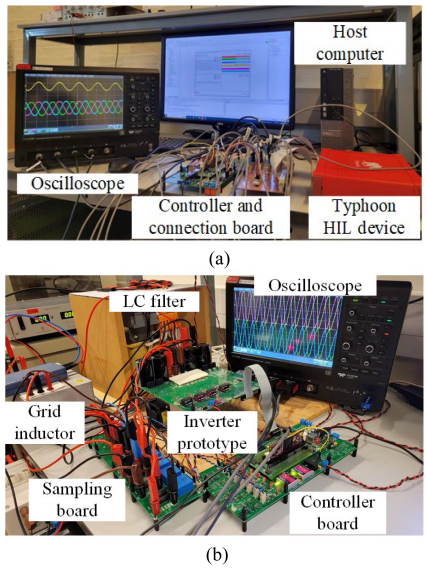

Fig. 13. Platforms for the HIL simulation and experiment. (a) HIL simulation. (b) Three-phase inverter prototype.

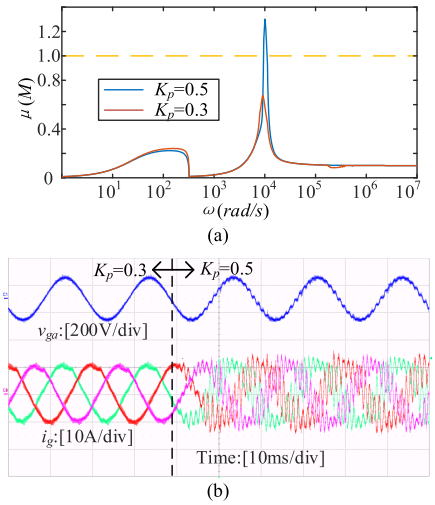

Fig. 14. Experimental verification of robust stability boundary. (a) Robust stability analysis with structured singular value. (b) Experimental verifications.

A. Verifications With Prototype

The physical prototype is used to verify the analysis of the stability boundary. The experimental verification of the robust stability boundary is shown in Fig. 14. The dc voltage for the experiment is 360 V. The grid voltage is provided by the regenerative grid simulator Chroma 61830 and the ac voltage is 110 V (RMS). The remaining nominal parameters are the same as that in Table II.

Because the parametric uncertainty in this article is between -1 to 1, the criterion for robust stability is whether the structured singular value μ is greater than 1 [35]. In the experimental verifications, the d-axis and q-axis regulators are the same and the proportional coefficient is recorded as K_p. When K_p is 0.3 and 0.5, the maximum SSVs are calculated as 0.67 and 1.3,

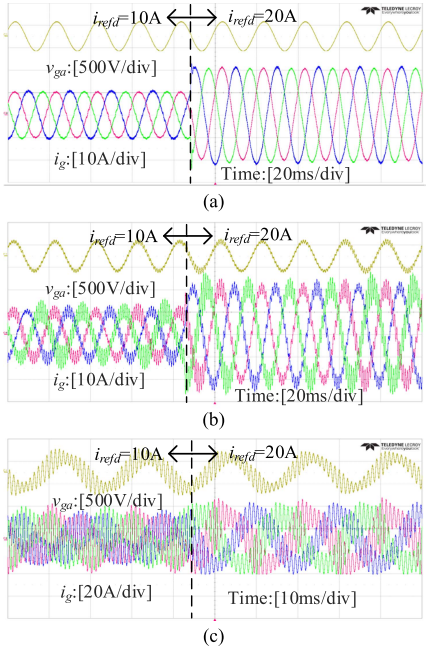

Fig. 15. Robust stability verification with filter capacitance change. (a) Within the stability boundary (10 μF). (b) Around the stability boundary (14 μF). (c) Beyond the stability boundary (15 μF).

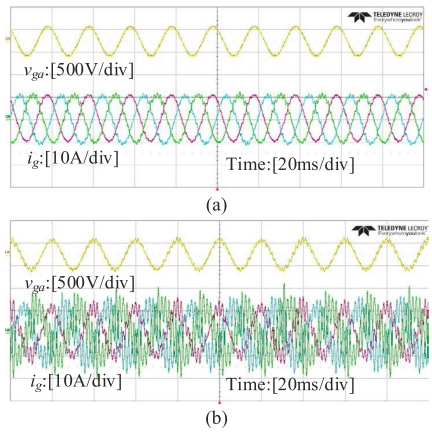

Fig. 16. Robust stability verification with grid inductance change. (a) Around the stability boundary (2 mH). (b) Beyond the stability boundary (3 mH).

respectively. According to the analysis results, the inverter is stable when $K_p = 0.3$, and the SSV exceeds the stability boundary when $K_p = 0.5$. The corresponding experimental verification waveforms are shown in Fig. 14(b) and the experimental results are consistent with the SSV analysis. The experimental results verify the correctness of the robust stability analysis.

B. Verifications With HIL Simulation

Because the component parameters can be changed arbitrarily in the HIL simulation, the influence of parameter variations is verified through the HIL simulation platform. Keeping the proportional coefficient at 0.3, the robust stability verification with the filter capacitance change is shown in Fig. 15. The filter

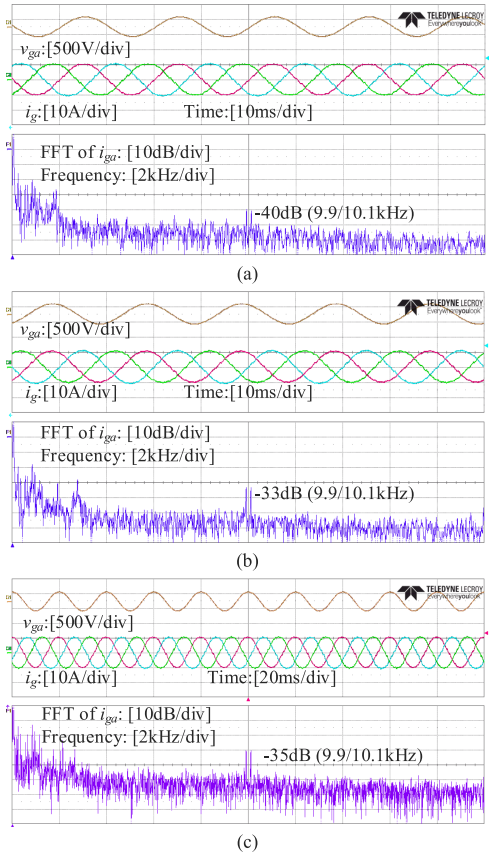

Fig. 17. HIL simulation waveforms and FFT analysis for filter performance verification. (a) Nominal operation. (b) Less filter capacitance (6 μF). (c) Less grid inductance (0.6 mH).

capacitors in Fig. 15(a)–(c) are 10, 14, and 15 μF, respectively, corresponding to the conditions within, around and beyond the stability boundary. The risk of instability increases with increasing capacitance, which is consistent with the analysis in Fig. 9(a). What's more, the current reference $i_{\mathrm{ref}\,d}$ is changed from 10 to 20 A in Fig. 15, which also verifies the robust performance of the system when the load changes.

The influence of the grid inductance variation is also verified through the HIL simulation. The corresponding HIL simulation results are shown in Fig. 16. The grid inductors in Fig. 16(a) and (b) are 2 and 3 mH, respectively. The waveform under nominal parameters is the same as that in the Fig. 15(a), so only the waveforms around and beyond the stability boundary are shown in Fig. 16. It can be seen that the increase of grid inductance will increase the risk of instability, which is also consistent with the analysis in case study.

The verification of the filter performance with uncertain parameters is shown in Fig. 17. When the filter capacitance decreases, the harmonic distortions around the switching frequency are -33 dB as shown in Fig. 17(b), and the harmonic distortions are significantly higher than those in Fig. 17(a) which is -40 dB. When the grid inductance decreases, the harmonic distortions around the switching frequency are -35 dB in Fig. 17(c), also higher than those in Fig. 17(a). Therefore, the filter performance is worse with less filter capacitance or grid

$$\boldsymbol{A}=\begin{bmatrix} 0 & -\omega & 0 & 0 & -1/L_1 & 0 & 0 & 0 & K_{\text{pwm}}/L_1 & 0 \\ \omega & 0 & 0 & 0 & 0 & -1/L_1 & 0 & 0 & 0 & K_{\text{pwm}}/L_1 \\ 0 & 0 & -R_g/L_g & -\omega & 1/L_g & 0 & 0 & 0 & 0 & 0 \\ 0 & 0 & \omega & -R_g/L_g & 0 & 1/L_g & 0 & 0 & 0 & 0 \\ 1/C_f & 0 & -1/C_f & 0 & 0 & -\omega & 0 & 0 & 0 & 0 \\ 0 & 1/C_f & 0 & -1/C_f & \omega & 0 & 0 & 0 & 0 & 0 \\ 0 & 0 & -K_{id} & 0 & 0 & 0 & 0 & 0 & 0 & 0 \\ 0 & 0 & 0 & -K_{iq} & 0 & 0 & 0 & 0 & 0 & 0 \\ -K_c/T_d & 0 & (K_c-K_{pd})/T_d & \omega L_g/T_d & 0 & 0 & 1/T_d & 0 & -1/T_d & 0 \\ 0 & -K_c/T_d & -\omega L_g/T_d & (K_c-K_{pd})/T_d & 0 & 0 & 0 & 1/T_d & 0 & -1/T_d \end{bmatrix} \tag{A1.3}$$

$$\boldsymbol{C}_1=\begin{bmatrix} 0 & 0 & 0 & 0 & -1/L_1 & 0 & 0 & 0 & K_{\text{pwm}}/L_1 & 0 \\ 0 & 0 & 0 & 0 & 0 & -1/L_1 & 0 & 0 & 0 & K_{\text{pwm}}/L_1 \\ 0 & 0 & -R_g/L_g & 0 & 1/L_g & 0 & 0 & 0 & 0 & 0 \\ 0 & 0 & 0 & -R_g/L_g & 0 & 1/L_g & 0 & 0 & 0 & 0 \\ 1/C_f & 0 & -1/C_f & 0 & 0 & 0 & 0 & 0 & 0 & 0 \\ 0 & 1/C_f & 0 & -1/C_f & 0 & 0 & 0 & 0 & 0 & 0 \end{bmatrix} \tag{A2.3}$$

inductance. The HIL simulation results are consistent with the analysis in Fig. 9(b).

VI. Conclusion

This article proposes a probabilistic framework for the failure risk assessment of grid-connected inverters, which quantifies the operational risk of grid-connected inverters in combination with multiparameter uncertainties. A case study on a three-phase inverter is performed to verify the proposed framework through HIL simulation and physical prototype testing. The results of failure risk analysis and assessment conduct the following conclusions.

1) The stability criterion of SSV less than 1 and the filter performance criterion of THD less than 5% are effective. The assessment results with the proposed criteria are consistent with the experimental verification.
2) The proposed probabilistic assessment framework quantifies the failure risk of inverters affected by environmental stress. It reveals from the case study that the increase of 5 °C or 5% relative humidity will accelerate the failure process of the inverter for about 6 years.
3) Based on the parametric sensitivity analysis, the redesigned case with a higher filter inductance ($1.2\,L_1$) can limit the risk of THD exceeding to less than 1.0% without increasing the instability risk.

Appendix A

The corresponding matrices in (12) are as follows (A1.3) shown at the top of this page

$$\boldsymbol{B}=\begin{bmatrix} 0 & 0 & -1/L_g & 0 & 0 & 0 & 0 & 0 & 0 & 0 \\ 0 & 0 & 0 & -1/L_g & 0 & 0 & 0 & 0 & 0 & 0 \\ 0 & 0 & 0 & 0 & 0 & 0 & K_{id} & 0 & K_{pd}/T_d & 0 \\ 0 & 0 & 0 & 0 & 0 & 0 & 0 & K_{iq} & 0 & K_{pd}/T_d \end{bmatrix}^{\mathrm{T}} \tag{A1.1}$$

$$\boldsymbol{C}=\begin{bmatrix} 0 & 0 & 1 & 0 & 0 & 0 & 0 & 0 & 0 & 0 \\ 0 & 0 & 0 & 1 & 0 & 0 & 0 & 0 & 0 & 0 \end{bmatrix}. \tag{A1.2}$$

Appendix B

The corresponding matrices in (15) are as follows (A2.3) shown at the top of this page

$$\boldsymbol{D}_{11}=\text{diag}\left(-P_1,-P_1,-P_g,-P_g,-P_c,-P_c\right) \tag{A2.1}$$

$$\boldsymbol{B}_1=\begin{bmatrix}\boldsymbol{D}_{11}\\ \boldsymbol{O}_1\end{bmatrix}. \tag{A2.2}$$

The matrix $\boldsymbol{O}_1$ has 4 rows and 6 columns, and all elements of $\boldsymbol{O}_1$ are 0.

References

[1] F. Blaabjerg, Z. Chen, and S. B. Kjaer, "Power electronics as efficient interface in dispersed power generation systems," *IEEE Trans. Power Electron.*, vol. 19, no. 5, pp. 1184–1194, Sep. 2004.

[2] M. Ferber, A. Korniienko, G. Scorletti, C. Vollaire, F. Morel, and L. Krahenbuhl, "Systematic LFT derivation of uncertain electrical circuits for the worst-case tolerance analysis," *IEEE Trans. Electromagn. Compat.*, vol. 57, no. 5, pp. 937–946, Oct. 2015.

[3] H. Wang et al., "Transitioning to physics-of-failure as a reliability driver in power electronics," *IEEE J. Emerg. Sel. Topics Power Electron.*, vol. 2, no. 1, pp. 97–114, Mar. 2014.

[4] R. Rosso, J. Cassoli, G. Buticchi, S. Engelken, and M. Liserre, "Robust stability analysis of *LCL* filter based synchronverter under different grid conditions," *IEEE Trans. Power Electron.*, vol. 34, no. 6, pp. 5842–5853, Jun. 2019.

[5] S. Li and H. Lin, "A capacitor-current-feedback positive active damping control strategy for *LCL*-type grid-connected inverter to achieve high robustness," *IEEE Trans. Power Electron.*, vol. 37, no. 6, pp. 6462–6474, Jun. 2022.

[6] Y. He, X. Wang, X. Ruan, D. Pan, and K. Qin, "Hybrid active damping combining capacitor current feedback and point of common coupling voltage feed-forward for *LCL*-type grid-connected inverter," *IEEE Trans. Power Electron.*, vol. 36, no. 2, pp. 2373–2383, Feb. 2021.

[7] C. R. D. Osorio, G. G. Koch, H. Pinheiro, R. C. L. F. Oliveira, and V. F. Montagner, "Robust current control of grid-tied inverters affected by *LCL* filter soft-saturation," *IEEE Trans. Ind. Electron.*, vol. 67, no. 8, pp. 6550–6561, Aug. 2020.

[8] T. Wu, M. Misra, Y. Jhang, Y. Huang, and L. Lin, "Direct digital control of single-phase grid-connected inverters with *LCL* filter based on inductance estimation model," *IEEE Trans. Power Electron.*, vol. 34, no. 2, pp. 1851–1862, Feb. 2019.
[9] E. B. Ssekulima, M. B. Anwar, A. Al Hinai, and M. S. El Moursi, "Wind speed and solar irradiance forecasting techniques for enhanced renewable energy integration with the grid: A review," *IET Renew. Power Gen.*, vol. 10, no. 7, pp. 885–989, Jul. 2016.
[10] X. Wang, Y. He, D. Pan, H. Zhang, Y. Ma, and X. Ruan, "Passivity enhancement for *LCL*-filtered inverter with grid current control and capacitor current active damping," *IEEE Trans. Power Electron.*, vol. 37, no. 4, pp. 3801–3812, Apr. 2022.
[11] Z. Xie, Y. Chen, W. Wu, W. Gong, and J. M. Guerrero, "Stability enhancing voltage feed-forward inverter control method to reduce the effects of phase-locked loop and grid impedance," *IEEE J. Emerg. Sel. Topics Power Electron.*, vol. 9, no. 3, pp. 3000–3009, Jun. 2021.
[12] L. Huang, H. Xin, and F. Dorfler, "H_∞-control of grid-connected converters: Design, objectives and decentralized stability certificates," *IEEE Trans. Smart Grid*, vol. 11, no. 5, pp. 3805–3816, Sep. 2020.
[13] Y. Wang, X. Wang, F. Blaabjerg, and Z. Chen, "Harmonic instability assessment using state-space modeling and participation analysis in inverter-fed power systems," *IEEE Trans. Ind. Electron.*, vol. 64, no. 1, pp. 806–816, Jan. 2017.
[14] N. Cifuentes, M. Sun, R. Gupta, and B. C. Pal, "Black-box impedance-based stability assessment of dynamic interactions between converters and grid," *IEEE Trans. Power Syst.*, vol. 37, no. 4, pp. 2976–2987, Jul. 2022.
[15] Z. Zeng et al., "An improved impedance modeling method of grid-tied inverters with white-box property," *IEEE Trans. Power Electron.*, vol. 37, no. 4, pp. 3980–3989, Apr. 2022.
[16] H. Gholami-Khesht, P. Davari, M. Novak, and F. Blaabjerg, "A probabilistic framework for the robust stability and performance analysis of grid-tied voltage source converters," *Appl. Sci.*, vol. 12, no. 15, Jul. 2022, Art. no. 7375.
[17] N. Rashidi, Q. Wang, R. Burgos, C. Roy, and D. Boroyevich, "Multi-objective design and optimization of power electronics converters with uncertainty quantification—Part I: Parametric uncertainty," *IEEE Trans. Power Electron.*, vol. 36, no. 2, pp. 1463–1474, Feb. 2021.
[18] D. Zhou, Y. Song, Y. Liu, and F. Blaabjerg, "Mission profile based reliability evaluation of capacitor banks in wind power converters," *IEEE Trans. Power Electron.*, vol. 34, no. 5, pp. 4665–4677, May 2019.
[19] A. Sangwongwanich, Y. Yang, D. Sera, and F. Blaabjerg, "Mission profile-oriented control for reliability and lifetime of photovoltaic inverters," *IEEE Trans. Ind. Appl.*, vol. 56, no. 1, pp. 601–610, Jan./Feb. 2020.
[20] E. Kaufhold, J. Meyer, S. Muller, and P. Schegner, "Probabilistic stability analysis for commercial low power inverters based on measured grid impedances," in *Proc. Int. Conf. Power Energy Syst.*, 2019, pp. 1–6.
[21] Y. Chen, S. Pan, M. Huang, H. Wang, H. Wang, and X. Zha, "Robust stability assessment of single-phase inverter with multiparameter distributions," *IEEE Trans. Power Electron.*, vol. 37, no. 5, pp. 6062–6073, May 2022.
[22] T. Tang and T. Zhou, "Recent developments in high order numerical methods for uncertainty quantification (in Chinese)," *Sci. Sinica Math.*, vol. 45, no. 7, pp. 891–928, 2015.
[23] TDK, Film Capacitors, "Metallized polypropylene film capacitors (MKP) [EB/OL]," 2018, [Online]. Available: https://product.tdk.com/en/system/files?file=dam/doc/product/capacitor/film/mkp_mfp/data_sheet/20/20/db/fc_2009/mkp_b32671z_676z.pdf
[24] Hammond Manufacturing, "Heavy current chassis mount 195-196 series [EB/OL]," 2022, [Online]. Available: https://www.hammfg.com/electronics/transformers/choke/195-196.pdf
[25] Q. Sun, Y. Tang, J. Feng, and T. Jin, "Reliability assessment of metallized film capacitors using reduced degradation test sample," *Qual. Reliab. Engng. Int.*, vol. 29, no. 2, pp. 259–265, Mar. 2013.
[26] Z. Özkan and A. M. Hava, "Inductor saturation compensation in three-phase three-wire voltage-source converters via inverse system dynamics," *IEEE Trans. Ind. Electron.*, vol. 69, no. 5, pp. 4309–4319, May 2022.
[27] Kool Mu Material Curves, Fit Formula of Toroid Cores, "Magnetics," [EB/OL]. 2019, [Online]. Available: https://www.mag-inc.com/Products/Powder-Cores/Kool-Mu-Cores/Kool-Mu-Material-Curves
[28] P. K. Janert, *Data Analysis With Open Source Tools: A Hands-On Guide for Programmers and Data Scientists*, Sebastopol, CA, USA: O'Reilly Media, 2010.
[29] D. Zhou, H. Wang, and F. Blaabjerg, "Reactive power impacts on *LCL* filter capacitor lifetime in grid-connected inverter," *IEEE Open J. Power Electron.*, vol. 1, pp. 139–148, 2020.
[30] H. Wang, P. Diaz Reigosa, and F. Blaabjerg, "A humidity-dependent lifetime derating factor for DC film capacitors," in *Proc. IEEE Energy Convers. Congr. Expo.*, 2015, pp. 3064–3068.
[31] Z. Shen, M. Chen, H. Wang, X. Wang, and F. Blaabjerg, "EMI filter robustness in three-level active neutral-point-clamped inverter," *IEEE Trans. Power Electron.*, vol. 37, no. 4, pp. 4641–4657, Apr. 2022.
[32] W. Ma, Y. Guan, B. Zhang, and L. Wu, "Active disturbance rejection control based single current feedback resonance damping strategy for *LCL*-type grid-connected inverter," *IEEE Trans. Energy Convers.*, vol. 36, no. 1, pp. 48–62, Mar. 2021.
[33] D. G. Holmes, T. A. Lipo, B. P. McGrath, and W. Y. Kong, "Optimized design of stationary frame three phase AC current regulators," *IEEE Trans. Power Electron.*, vol. 24, no. 11, pp. 2417–2426, Nov. 2009.
[34] K. Zhou, J. Doyle, and K. Glover, *Robust and Optimal Control*. Englewoo Cliffs, NJ, USA: Prentice-Hall, 1996.
[35] S. Sumsurooah, M. Odavic, S. Bozhko, and D. Boroyevich, "Robust stability analysis of a DC/DC buck converter under multiple parametric uncertainties," *IEEE Trans. Power Electron.*, vol. 33, no. 6, pp. 5426–5441, Jun. 2018.
[36] R. Pena-Alzola, M. Liserre, F. Blaabjerg, M. Ordonez, and Y. Yang, "*LCL*-filter design for robust active damping in grid-connected converters," *IEEE Trans. Ind. Inf.*, vol. 10, no. 4, pp. 2192–2203, Nov. 2014.

Yongyang Chen (Student Member, IEEE) was born in Hefei, Anhui Province, China, in 1996. He received the B.Eng. degree in electrical engineering in 2017 from Wuhan University, Wuhan, China, where he is currently working toward the Ph.D. degree.

He was a Visiting Student with the Aalborg University, Aalborg, Denmark, from December 2021 to October 2022. His main research interests include the modular multilevel converter and robustness analysis of power converters.

Ariya Sangwongwanich (Member, IEEE) received the B.Eng. degree in electrical engineering from Chulalongkorn University, Thailand, in 2013, and the M.Sc. and Ph.D. degrees in energy engineering from Aalborg University, Denmark, in 2015 and 2018, respectively.

He is currently an Assistant Professor with the Department of Energy Technology, Aalborg University, where he is a Vice-Leader of Photovoltaic Systems research program. His research interests include control of grid-connected converters, photovoltaic systems, reliability in power electronics, and multi-level converters. He was a Visiting Researcher with RWTH Aachen, Aachen, Germany in 2017 and University of Cambridge, Cambridge, United Kingdom in 2023.

Dr. Sangwongwanich was the recipient of the Danish Academy of Natural Sciences' Ph.D. Prize and the Spar Nord Foundation Research Award for his Ph.D. thesis in 2019.

Meng Huang (Member, IEEE) received the B.Eng. and M.Eng. degrees from the Huazhong University of Science and Technology, Wuhan, China, in 2006 and 2008, respectively, and the Ph.D. degree in power electronics from the Hong Kong Polytechnic University, Hong Kong, in 2013.

He is currently an Associate Professor with the School of Electrical Engineering and Automation, Wuhan University, Wuhan, China. His research interests lie in the safe operation and control of grid-connected systems.

Dr. Huang was the recipient of Best Paper Award of the IEEE TRANSACTIONS ON POWER ELECTRONICS in 2016. He is currently an Editor of *International Journal of Circuit Theory and Applications*, and was a Guest Editor for IEEE JOURNAL OF EMERGING AND SELECTED TOPICS OF CIRCUITS AND SYSTEMS, a Guest Associate Editor for IEEE TRANSACTIONS ON INDUSTRIAL APPLICATIONS and IEEE JOURNAL OF EMERGING AND SELECTED TOPICS OF POWER ELECTRONICS.

Shangzhi Pan (Senior Member, IEEE) received the B.Sc. and M.Sc. degrees in electrical engineering from Zhejiang University, China, in 1998 and 2001, respectively, and the Ph.D. degree in electrical engineering from Queen's University, Kingston, ON, Canada, in 2008.

In 2018, he was with the College of Electrical Engineering, Wuhan University, China, where he is currently a Professor. He has been currently an Adjunct Faculty with Queen's Center of Energy and Power Electronics Applied Research Laboratory (ePOWER), since 2014. Previously, he was as the VP of research and development at SPARQ systems, a Queen's Spun-off photovoltaic microinverter company since 2010. He was a Senior Research Engineer with Queen's University, from 2008 to 2013. His research interests include digital control techniques for power converters, grid-connected inverters, voltage regulators for computing systems, power converters for renewable energy sources, and power converters for electric vehicles.

Xiaoming Zha (Senior Member, IEEE) was born in Huaining, Anhui Province, China, in 1967. He received the B.S., M.S., and Ph.D. degrees in electrical engineering from Wuhan University, Wuhan, China, in 1989, 1992, and 2001, respectively.

He was a Postdoctoral Fellow with the University of Alberta, Edmonton, AB, Canada from 2001 to 2003. He has been a Faculty Member with Wuhan University, since 1992, and became a Professor in 2003. He is currently the Director of Hubei Key Laboratory of Power Equipment & System Security for Integrated Energy, Wuhan University, Wuhan, China. His research interests include power electronic converter, the application of power electronics in smart grid and renewable energy generation, the analysis and control of microgrid, the analysis and control of power quality, and frequency control of high- voltage high-power electric motors.

Huai Wang (Senior Member, IEEE) received the BE degree in electrical engineering from Huazhong University of Science and Technology, Wuhan, China, in 2007 and the Ph.D. degree in power electronics from the City University of Hong Kong, Hong Kong, in 2012.

He is currently Professor with AAU Energy, Aalborg University, Aalborg, Denmark, where he leads the group of Reliability of Power Electronic Converters (ReliaPEC) and the mission on Digital Transformation and AI. He was a Visiting Scientist with the ETH Zurich, Switzerland, from August to September 2014, and with the Massachusetts Institute of Technology, USA, from September to November 2013. He was with the ABB Corporate Research Center, Switzerland in 2009. His research addresses the fundamental challenges in modeling and validation of power electronic component failure mechanisms and application issues in system level predictability, condition monitoring, circuit architecture, and robustness design.

Dr. Wang was the recipient of the Richard M. Bass Outstanding Young Power Electronics Engineer Award from the IEEE Power Electronics Society in 2016, and the Green Talents Award from the German Federal Ministry of Education and Research in 2014. He is currently the Chair of IEEE PELS/IAS/IES Chapter in Denmark. He serves as an Associate Editor of IET Electronics Letters, IEEE JOURNAL OF EMERGING AND SELECTED TOPICS IN POWER ELECTRONICS, and IEEE TRANSACTIONS ON POWER ELECTRONICS.